

Implications of Pulse Sequence in Structural Imaging of Trabecular Bone

Arañee Techawiboonwong, BSE, Hee Kwon Song, PhD, Jeremy F. Magland, PhD, Punam K. Saha, PhD, and Felix W. Wehrli, PhD*

Purpose: To investigate the SNR and image properties of 3D steady-state free precession (SSFP), fast large-angle spin echo (FLASE), gradient-recalled acquisition in steady state (GRASS), and spoiled GRASS (SPGR) for structural imaging of trabecular bone (TB).

Materials and Methods: SNR was examined theoretically and experimentally on phantoms, bone specimens, and in vivo. The bone volume fraction, TB thickness, and echo time (TE) dependence of the thickness were compared. The trabecula was modeled as a cylinder in simulations to examine the intravoxel spin-dephasing in SSFP and GRASS. Images were acquired on a 1.5T Siemens Sonata system (40 mT/m maximum gradient, 200 T/m/s peak slew rate).

Results: Within the hardware and safety limit constraints, SNR of FLASE was superior, followed by SSFP, GRASS, and SPGR. The trabecular thickness derived from gradient-echo images was 10–45% greater than that obtained with FLASE. Conversely, SSFP images delineated partial volume trabeculae better than FLASE. Simulations indicated that the artifactual thickening was more severe in SSFP than in GRASS, which was attributed to off-resonance effects from the induced gradients at the bone/marrow interface.

Conclusion: FLASE had the highest SNR and was insensitive to susceptibility dephasing. Although SSFP has superior SNR compared to GRASS, off-resonance effects and duty cycle limitations may compromise its practicality in this application.

Key Words: trabecular bone; micro-MRI; SSFP; FLASE; susceptibility

J. Magn. Reson. Imaging 2005;22:647–655.

© 2005 Wiley-Liss, Inc.

OSTEOPOROSIS IS a metabolic bone disease that is characterized by bone loss and architectural deteriora-

tion. The most common method for fracture risk assessment is the measurement of bone mineral density (BMD), typically by means of dual-energy X-ray absorptiometry (DXA). In fact, bone strength is determined by its mass and composition, and, most notably, its architecture. However, bone densitometry cannot provide any information about bone architecture, which is key to assessing fracture risk (1,2). Since most osteoporotic fractures occur at locations that are rich in trabecular bone (TB), imaging modalities that can provide sufficient resolution to resolve individual trabeculae are required for assessment of TB architecture. Recent advances in high-resolution MRI (μ -MRI) now permit in vivo imaging at a resolution of ~ 100 – $200 \mu\text{m}$ (3,4), which is on the order of TB thickness (5).

TB consists of a connected network of bony struts and plates interspersed with fatty (yellow) or hematopoietic (red) marrow. In MR images bone has low intensity, by virtue of bone water's extremely short T_2 (~ 250 – $500 \mu\text{s}$) (6), while marrow appears as a bright signal. Bone is also more diamagnetic than either fat or water. The susceptibility difference between bone and fatty marrow is approximately 3 ppm (in S.I. units) (7) and thus affects the local field distribution at the bone-marrow interface. In gradient-echo imaging the local magnetic field inhomogeneities lead to intravoxel phase dispersion and hence reduction of the signal (8,9). One manifestation of this effect is artifactual broadening of the trabeculae (10,11).

Currently, the two primary techniques used for μ -MRI of TB are variants of the basic gradient-echo (gradient-recalled acquisition in steady state (GRASS) and spoiled GRASS (SPGR)) and spin-echo-based fast large-angle spin-echo (FLASE) pulse sequences (3,4). Although it is not currently used for structural imaging of TB, steady-state free precession (SSFP) has recently proven its potential in various applications because of its short scan time and high SNR efficiency (12–15). SSFP is essentially a gradient-echo sequence in which TR is chosen to be as short as technically feasible, and imaging gradients in all directions are fully rewound at the end of each repetition period. SSFP is known to be highly sensitive to off-resonance effects resulting from field inhomogeneity and chemical shift dispersion (16). However, recent advances in magnet and shimming technology that enable extremely uniform B_0 fields

Laboratory for Structural NMR Imaging, Department of Radiology, University of Pennsylvania Medical Center, Philadelphia, Pennsylvania, USA.
Contract grant sponsor: NIH; Contract grant numbers: RO1 AR 49553; RO1 AR 41443.

*Address reprint requests to: F.W.W., Department of Radiology, University of Pennsylvania Medical Center, 3400 Spruce Street, 1 Founders, MRI Education Center, Philadelphia, PA 19104.
E-mail: wehrli@uphs.upenn.edu

Received December 22, 2004; Accepted July 29, 2005.

DOI 10.1002/jmri.20432

Published online 7 October 2005 in Wiley InterScience (www.interscience.wiley.com).

along with faster and stronger gradients now make SSFP practical. Thus, SSFP could provide an alternative technique for μ -MRI of TB that is worth exploring.

The fundamental difference between spin echo (RF echo) and gradient echo is the manner in which the echo is formed. An RF echo is obtained with a phase reversal RF pulse along with balancing of the read gradient. Hence, at echo time (TE) the isochromats are in phase. On the other hand, the gradient echo is formed when the gradient zeroth moments are balanced, at which time the isochromats are not necessarily in phase. In fact, each isochromat acquires a phase that depends on the local field it experienced between excitation and detection. Another source of destructive interference of isochromats at TE is chemical shift. Fatty marrow (which prevails in the distal extremities) is composed of fatty acid triglycerides that possess multiple chemically-shifted resonances. The fundamental difference between the two families of sequences suggests that RF-echo-based pulse sequences are more appropriate for imaging regions that are prone to susceptibility-induced local fields and chemical shift dispersion, such as in TB marrow. Although the phase dispersion is eliminated in the spin echo, the signal decays as $\exp(-TE/T_2)$. The use of a phase reversal pulse may require a significantly longer time to form an echo compared to a gradient echo—a consideration that would favor gradient-echo-based pulse sequences.

Earlier work demonstrated that spin-echo-based FLASE has significantly higher SNR efficiency compared to GRASS (17). The goal of the current work was to evaluate the performance and practicality of the SSFP sequence in comparison with the existing 3D imaging techniques for μ -MRI of TB. The performance of the algorithm used to extract the structural parameters is critically dependent on SNR and overall image quality, the two criteria examined in this work (18).

MATERIALS AND METHODS

Overview of Pulse Sequences Examined

The 3D gradient- and spin-echo-based pulse sequences investigated were 1) FLASE, 2) SSFP (also referred to as TrueFISP), 3) GRASS (also referred to as FISP), and 4) SPGR. The fundamentals of each sequence and the conditions under which SNR was maximized are briefly summarized below.

Spin-Echo Sequence

The 3D FLASE sequence is a modification of a spin-echo sequence that is optimized for short-TR applications (17). The sequence, shown in Fig. 1, utilizes a large excitation flip angle ($>90^\circ$) to partially invert the magnetization while creating a transverse component. The phase-reversal pulse then restores the longitudinal component while generating an echo from the transverse component. It is essentially a spin-echo equivalent of a small-tip-angle, fast gradient-echo sequence. The optimum excitation flip angle of FLASE to maximize SNR is approximately $(\pi - \alpha_E)$ where $\alpha_E = \cos^{-1}(\exp(-TR/T_1))$ is the Ernst angle. In the present implementation a large-angle, minimum-phase Shinnar-Le Roux (19) ex-

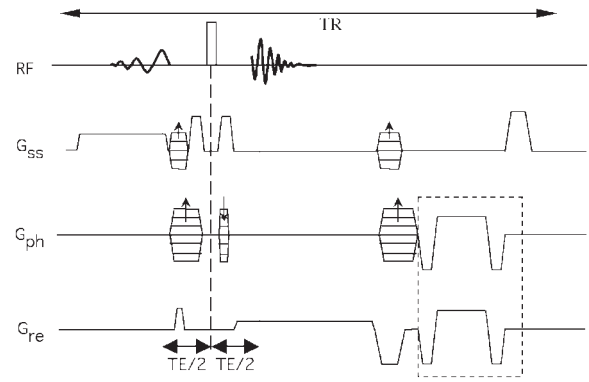


Figure 1. FLASE pulse sequence diagram, with the dashed region indicating navigator readouts alternating between the read and phase-encoding axes. See text for further details.

citation was used in conjunction with a nonselective refocusing pulse to minimize TE. TE was further minimized by performing a partial k-space acquisition in the readout direction, and by splitting the phase-encoding gradient to either side of the refocusing pulse. Additionally, the sequence used alternating navigator readouts to correct for in-plane translational motion artifacts (20).

The FLASE transverse magnetization can be expressed as (17):

$$M_{xy}(TR, TE, \alpha, T_1, T_2) = M_0 \sin \alpha \exp\left(\frac{-TE}{T_2}\right) \cdot \left\{ 1 - 2E_1 \exp\left(\frac{TE}{2T_1}\right) + E_1 \right\} \cdot f'(\beta, \alpha) \quad (1)$$

$$f' \equiv (1 + E_2 \cos \beta) / [(1 + E_1 \cos \alpha)(1 + E_2 \cos \beta) - (E_1 + \cos \alpha)(E_2 + \cos \beta)E_2] \quad (2)$$

where $E_1 \equiv \exp(-TR/T_1)$, $E_2 \equiv \exp(-TR/T_2)$, α is the excitation flip angle, and β is the resonance offset angle due to the presence of background field inhomogeneity ΔB and the fields induced by the time-dependent imaging gradients, $G(t)$, the isochromats experienced at each location, given by the expression

$$\beta(x, y, z, TR) = \gamma \Delta B(x, y, z) \cdot TR + \gamma \vec{r} \cdot \int_0^{TR} \vec{G}(t) dt \quad (3)$$

The use of sufficiently large killer gradients at the end of each TR period causes β to become uniformly distributed across the voxel, and thus it is no longer a function of position.

Gradient-Echo Sequences

The 3D gradient-echo based SSFP, GRASS, and SPGR sequences employ the same imaging gradient structure, with the following distinguishing features: 1) in SSFP all imaging gradients are fully rewound within each TR period (21); 2) GRASS uses phase-and slice-

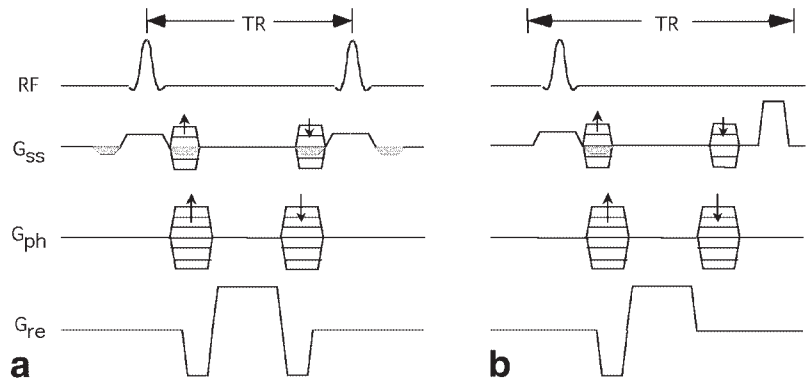


Figure 2. The 3D gradient-echo pulse sequences used. SSFP (a) differs from GRASS (b) only in the readout rewinder.

encoding rewinders, complemented by a killer gradient that is typically applied along the slice-select direction to dephase any remaining magnetization at the end of each TR period (22); and 3) SPGR uses RF spoiling, which is achieved by advancing the RF phase from cycle to cycle (23,24), but is otherwise identical to the GRASS sequence. The fully balanced gradients in SSFP provide benefits from signal combined from multiple coherence pathways, but it is well known to be sensitive to off-resonance effects. By contrast, the killer gradients and the spoiling mechanism in GRASS and SPGR minimize potential artifacts due to stimulated-echo and off-resonance effects, albeit at the expense of lower SNR, especially when $TR \ll T_2$. The optimum flip angle in SSFP is a function of several factors, including TR, T_1 , T_2 , and resonance offset angle β (21). The optimum flip angle in GRASS can be determined numerically for a given set of imaging parameters, while that of SPGR is simply the Ernst angle.

The timing diagram for the gradient-echo sequence is shown in Fig. 2, and the transverse magnetization of each isochromat was previously derived by (21):

$$M_{xy}(TR, TE, \alpha, T_1, T_2) = M_0(1 - E_1) \sin \alpha \sqrt{1 + E_2^2 - 2E_2 \cos \beta} / D \cdot \exp\left(-\frac{TE}{T_2}\right) \quad (4)$$

$$D = (1 - E_1 \cos \alpha)(1 - E_2 \cos \beta) - (E_1 - \cos \alpha)(E_2 - \cos \beta)E_2 \quad (5)$$

In the case of SSFP, where all imaging gradients are fully rewound at the end of TR, $\int_0^{TR} \vec{G}(t) dt = 0$, β becomes solely dependent on ΔB and TR. It is obvious that for $T_2 \ll TR$ or the use of RF spoiling, Eq. [4] reverts to the simple expression that is valid for SPGR.

SNR Performance

The relative efficiency of each pulse sequence was evaluated in terms of the achievable SNR per unit scan time:

$$SNR \propto \Delta x \Delta y \Delta z \cdot f_{seq}(T_1, T_2, TR, TE) \cdot \sqrt{\frac{T_s}{TR}} \quad (6)$$

where $\Delta x \Delta y \Delta z$ is the voxel volume; f_{seq} is a parameter representing the magnetization of each individual sequence weighted by T_1 , T_2 , TR, and TE; and T_s is the duration of the readout gradient (also referred to as the sampling time) in each repetition period. SNR was measured experimentally and calculated from the respective equations (Eqs. [1]–[5]), normalized by multiplication with the square root of the ratio of the sampling time to the TR to obtain the SNR per unit scan time.

Image Acquisition

The performance of the various pulse sequences was evaluated in terms of SNR efficiency, sensitivity to artifacts, and their effects on the derived structural parameters. The performance was also compared in vivo among the sequences in the distal radius.

SNR Comparison in Phantom

SNR efficiency was first evaluated using two homogeneous phantoms: 1) edible oil to mimic fatty marrow, and 2) gadolinium-doped agarose with T_1 and T_2 similar to that of fatty marrow. In contrast to oil, water represents a simpler system that consists of only a single spectral resonance that is not susceptible to off-resonance dephasing. The measured T_1/T_2 values were 184/40 msec and 175/54 msec for the oil and water phantoms, respectively. Both phantoms were scanned with all four sequences. Voxel size was kept at $137 \times 137 \times 410 \mu\text{m}^3$ (FOV = $7 \times 5.25 \text{ cm}^2$, matrix size = $512 \times 384 \times 32$), consistent with current trabecular imaging protocols at the authors' institution (4), while other parameters were varied to optimize SNR (the minimum TE and TR are limited by hardware, i.e., slew rate and gradient duty cycle). In a short-TR sequence, the gradient duty cycle is significantly determined by the sampling time and thus the receiver bandwidth. For SSFP, the maximum receiver bandwidth allowed by the gradient duty cycle was used, whereas for GRASS and SPGR it was adjusted such that their TEs were as close as possible to that of SSFP so that the gradient-echo-based sequences could be compared under identical conditions. The low bandwidth that is possible in FLASE favors this pulse sequence. It should be noted that this latitude in the choice of bandwidth is not available in the gradient-echo-based sequences. SSFP owes its high SNR efficiency to the coherences across

Table 1
Imaging Parameters for Phantom and Intact Specimen Imaging

| | FLASE | SSFP | GRASS | SPGR |
|--|------------------|------------|------------|------|
| TE (msec) | 9.5 ^a | 7.9 | 8.2 | 8.2 |
| TR (msec) | 80 | 15.8 | 17 | 17 |
| Flip angle (deg) | 140 | 48 | 36 | 24 |
| BW_read (Hz/ pixel) | 32 | 130 | 160 | 160 |
| N _{avg} ^b (phantom/ specimen) | 1/1 | 1/5 | 1/5 | 1 |
| T _{scan} (minutes: seconds) | 16:25 | 3:15/16:30 | 3:30/17:20 | 3:30 |

^aPartial Fourier acquisition.

^bDue to gradient heating issues, the five N_{avg} scans were acquired separately and subsequently combined, allowing a cooling period between the acquisitions.

multiple pulse sequence cycles, which requires that the condition $TR \ll T_2$ be satisfied. Further, the sensitivity to off-resonance artifacts in SSFP is exacerbated at increased TR. Therefore, the SNR comparisons were conducted in the regime of optimum performance specific to each sequence. The total scan time for each sequence was on the order of 17 minutes. The scan parameters are given in Table 1. The partial-Fourier data collected from FLASE were reconstructed using a complex conjugation technique with low-order phase correction (25). All imaging experiments were performed on a 1.5 Tesla Siemens Sonata system equipped with 40 mT/m maximum gradient amplitude and 200 T/m/second maximum gradient slew rate using an in-house-built transmit/receive elliptical birdcage wrist coil (4).

Measurements in TB Specimens

The purpose of these experiments was to evaluate the dependence of the derived structural parameters on the specific pulse sequence used. Toward this end, human bone specimens were prepared. Two intact radii harvested from frozen cadavers were fixed in formalin (10%), placed in cylindrical plastic containers, and imaged with FLASE, SSFP, and GRASS. Further, to illustrate the TE dependence of apparent trabecular thickness affected by discontinuous susceptibility at the bone–bone marrow boundary (9,26–28), a demarrowed bone specimen was scanned with the same three sequences at multiple TEs. The specimen was immersed in 0.9 mM Gd-DTPA-doped water to yield $T_2 \sim 175$ msec (as opposed to ~ 60 msec in bone marrow) so that the inequality $TR \ll T_2$ in SSFP would hold.

Finally, to evaluate the potentially deleterious effects from multiple spectral peaks, the point-spread function (PSF) was measured in the bone marrow of one of the intact specimens of radial TB. For this purpose, the FLASE pulse sequence was modified as a 2D spectroscopic imaging sequence by phase encoding in both the x and y directions and reading out the signal in the absence of gradients. The TR and TE were kept the same as for the imaging experiments to maintain the same steady-state signal. The matrix size was reduced to 64×64 to keep the scan time practical, with an FOV of 5×5 cm², yielding a 780×780 μm^2 pixel size. The

imaging slice was chosen approximately in the center of the scan volume, with a thickness of 10 mm. An average linewidth was computed from 100 pixels within a 10×10 ROI.

In Vivo TB Imaging

Based on the results from the phantom and bone specimen scans, the two best-performing sequences were chosen for in vivo experiments. High-resolution images of the distal radius were obtained in a healthy volunteer to compare the SSFP sequence with the FLASE sequence currently used in the authors' laboratory. The parameters were those shown in Table 1, except for the FOV (8×4.5 cm²) and slice thickness (500 μm), yielding a voxel size of $156 \times 156 \times 500$ μm^3 . To overcome limitations caused by gradient heating, SSFP was prescribed with two averages (N_{avg} = 2) and elliptical k-space coverage, reducing the total scan time to 3 minutes 50 seconds. To minimize the adverse effects of subject movement, the imaged limb was immobilized with the aid of a vacuum bag. In addition, the FLASE sequence used navigator echoes alternating between the x and y directions (transverse plane) to correct for translational displacements during the scan (20).

Image Analysis

The image SNR was computed as the ratio of the ROI mean within the TB region to the mean of the background noise. The MR-derived parameters of interest were bone volume fraction (BVF) and TB thickness. BVF was calculated using a histogram deconvolution algorithm (29) that results in a noiseless image in which pixel intensity represents the fractional bone content. TB thickness was computed from the BVF maps with the Fuzzy Distance Transform (FDT) method (30), which allows measurement of structural thickness in the limited-resolution regime.

Simulation

Although the spin dephasing mechanism in gradient-echo sequences has been studied widely (17,26, 27,31,32), the severity of artifactual TB thickening at a given TE may be pulse sequence-specific. To examine this phenomenon, a simple model was invoked to simulate the effect of static spin dephasing under the influence of local field distortions using IDL (RSI, Boulder, CO, USA) image processing software. The simulation results were then compared qualitatively to images obtained from a demarrowed bone sample immersed in doped water.

In brief, the induced local field surrounding an infinitely long cylindrical rod oriented perpendicular to the B₀ field (Fig. 3) was computed based on the explicit expression for the magnetization of each sequence using Eqs. [1]–[5]. Toward this goal, each of the 137×410 μm^2 pixels (the field is invariant along the cylinder axis) was subdivided into 1×1 μm^2 subpixels. For all sequences, the net voxel signal amplitude was computed by numerically integrating the complex magnetizations within each subvoxel at the TE:

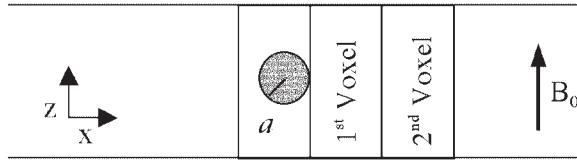


Figure 3. “Trabecula” modeled as a cylinder of 100 μm diameter perpendicular to the direction of the static field and tangential to the boundary of a $137 \times 410 \mu\text{m}^2$ pixel.

$$I(\text{voxel}) = \iiint_{\Delta v} M(x, y, z) e^{i\gamma \Delta B(x, y, z) TE} dx dy dz \quad (7)$$

The diameter of the rod (simulating a single trabecular element) was assumed to be 100 μm , with a susceptibility difference $\Delta\chi$ between bone and fatty marrow of 3 ppm S.I. (7). The model took into account only the effects of a single trabecular element, ignoring the effects from nearby trabeculae. This is not unrealistic considering that typical intertrabecular spacing is on the order of 300–600 μm (5), and further that $\Delta\chi \ll 1$. The magnetic field induced by a circular cylinder perpendicular to B_0 is given by (33):

$$\Delta B = \frac{\Delta\chi}{2} B_0 a^2 \frac{(z^2 - x^2)}{(z^2 + x^2)^2} \quad (8)$$

where a is the cylinder radius (Fig. 3). The signal intensity was then calculated for the voxels adjacent and second-nearest to the voxel encompassing the “trabecula.”

RESULTS

SNR Evaluation

The predicted and experimental SNRs for the four pulse sequences in the two homogenous phantoms (oil and doped water) and TB, normalized to the values of FLASE, are listed in Table 2. The measured values were in good agreement with the predictions indicating FLASE to be the most efficient sequence. A plot of predicted SNR as a function of TR for TB is shown in Fig. 4. The data indicate that the SNRs of GRASS and SPGR are comparable at $\text{TR} > 20$ msec, as expected, since the sequences behave similarly except when $\text{TR} \ll T_2$. The

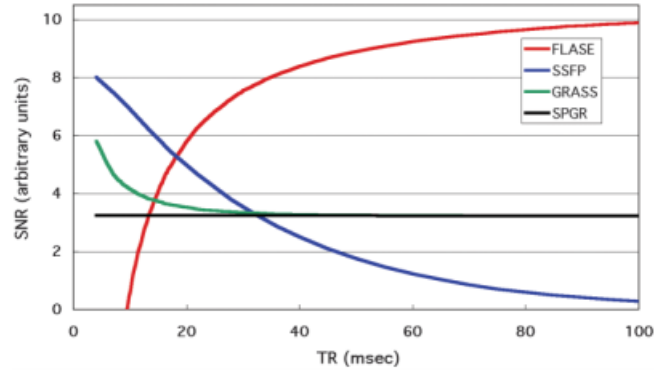


Figure 4. Dependence of normalized SNR on TR for four pulse sequences, assuming relaxation properties as encountered in the distal extremities where fatty marrow prevails ($T_1 = 300$ msec, $T_2 = 60$ msec, $T_2^* = 12$ msec). The simulation used optimum flip angles at each TR for all sequences. For SSFP, both TE and T_s were maintained at $\text{TR}/2$, while those of other sequences were kept at constant values as used experimentally.

subsequent structural parameter comparisons were therefore performed for the following three sequences: FLASE, SSFP, and GRASS.

Structural Parameters

The images of the intact distal radius specimen shown in Fig. 5 suggest a slight thickening of the trabeculae for SSFP and GRASS as compared to FLASE, although visually the effect is not dramatic. However, trabeculae that are partially or not at all visible in the FLASE images (because of partial volume averaging) become apparent in the gradient-echo images. This effect is likely caused by the greater attenuation of the signal in the voxel containing the trabecula as a consequence of the local gradients at the bone–bone marrow interface.

The results of the TB thickness and BVF measurements are summarized in Table 3. The data show that the TB is thicker on average by 10% and 45% in the gradient-echo based sequences (GRASS and SSFP, respectively) compared to FLASE. Commensurate with the greater apparent thickness, the BVF is substantially larger in SSFP and GRASS.

Lastly, the PSF was obtained as previously described within the TB region, with each pixel containing both

Table 2
Normalized Computed and Experimental SNR of the Homogenous Phantoms and Intact TB Specimens.*

| SNR | FLASE | SSFP | GRASS | SPGR |
|---------------------|-----------------------|-----------------|-----------------|-----------------|
| Computed | | | | |
| Doped water phantom | 1.0 | 0.96 | 0.63 | 0.58 |
| Oil phantom | 1.0 [0.92] | 0.55 | 0.38 | 0.36 |
| Intact TB specimen | 1.0 [0.71] | 0.59 | 0.38 | 0.34 |
| Experimental | | | | |
| Doped water phantom | 1.0 ± 0.08 | 0.99 ± 0.03 | 0.62 ± 0.02 | 0.60 ± 0.02 |
| Oil phantom | 1.0 ± 0.08 [1.01] | 0.52 ± 0.05 | 0.37 ± 0.03 | 0.28 ± 0.04 |
| Radius 1 | 1.0 ± 0.03 [0.69] | 0.65 ± 0.01 | 0.29 ± 0.01 | – |
| Radius 2 | 1.0 ± 0.01 [0.77] | 0.58 ± 0.02 | 0.27 ± 0.01 | – |

*SNR values in brackets are relative to doped water. The measurements were taken from multiple slices in the middle of the volume to minimize effects from B_1 inhomogeneity.

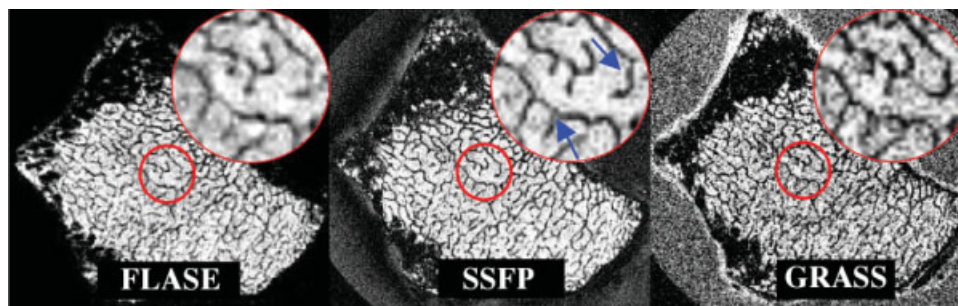


Figure 5. μ -MRI of intact distal radii obtained with different pulse sequences. Images were acquired in the same total scan time of approximately 17 minutes. Note that some trabecular elements that are not visible in the FLASE images are apparent in the SSFP and GRASS images (arrows).

fatty marrow and trabeculae (data not shown). All spectra consisted of two peaks separated by approximately 200 Hz, with the amplitude of the secondary peak being less than 10% of that of the primary peak. Other peaks had negligible amplitude. The average value of the linewidth from the 100 spectra was 50 ± 6 Hz, or roughly 1.6 pixels at the 32 Hz/pixel receiver bandwidth used.

TE Dependence of the Voxel Signal Amplitude in Simulation

In Fig. 6 the computed signal amplitude of the nearest and second-nearest voxels relative to the voxel containing the “trabecula” is plotted as a function of TE. The signal amplitude was calculated relative to a voxel that was not affected by susceptibility-induced field inhomogeneities. The simulation was performed with the “trabecula” positioned at the boundary rather than at the center of the voxel to simulate the worst-case effect on the adjacent (nearest neighbor) voxel signal. At TR = 16 msec, the phases across the voxel are 8.9 and 0.5 radians in the first and second adjacent voxels, increasing to 22.3 and 1.1 radians, respectively, at TR = 40 msec. It is noted that the SSFP signal amplitude of the adjacent voxel is attenuated by 28% at the experimental TE of 8 msec used in the intact specimens, and naturally the attenuation increases with increasing TEs. However, attenuation of the next-nearest voxel signal amplitude is negligibly small. In the voxel encompassing the trabecula, the FLASE signal is attenuated commensurately with the volume fraction occupied (14% in this case). However, in SSFP and GRASS the signal loss is as high as 84%. Finally, it is interesting to note that the relative signal loss of the first neighboring voxel in GRASS is less than that in SSFP. This observation is attributed to the use of a killer gradient in GRASS, which causes the off-resonance phase angles to become uniformly distributed across the voxel. The result is a generally lower absolute signal amplitude in GRASS relative to SSFP. However, the sequence becomes less sensitive to signal variations caused by susceptibility-induced inhomogeneities (16,21).

The artifactual TB thickening observed in the experiments conducted on intact bone (see Fig. 5 and Table 3) are in semiquantitative agreement with the simulations in that the dephasing-induced broadening was greater in the SSFP images than in the GRASS images.

Further support for the validity of the simulations is provided by the images acquired from a demarrowed specimen at two TEs (Fig. 7). The images highlight the TE-dependent trabecular thickening of both SSFP and GRASS, while the FLASE images appear to be insensitive to TE in this respect. Significant artifacts are visible with complete signal suppression at some locations, even at the shorter TE of 8 msec for both gradient-echo sequences. Areas of high signal in the FLASE images (obscured by local dephasing in the gradient-echo images) are attributed to signal mismapping from local susceptibility-induced gradients superimposed on the readout gradient (9).

In Vivo Images

The wrist images of a healthy volunteer acquired with FLASE and SSFP are shown in Fig. 8. The trabeculae clearly appear to be thicker in the SSFP images. Note the signal loss in the SSFP images, particularly near the radio-ulnar joint where trabeculation is particularly dense.

DISCUSSION

At the resolution required by the targeted application and the hardware constraints of a typical clinical imager, both theoretical projections and experimental data indicate that 3D FLASE is superior in terms of SNR

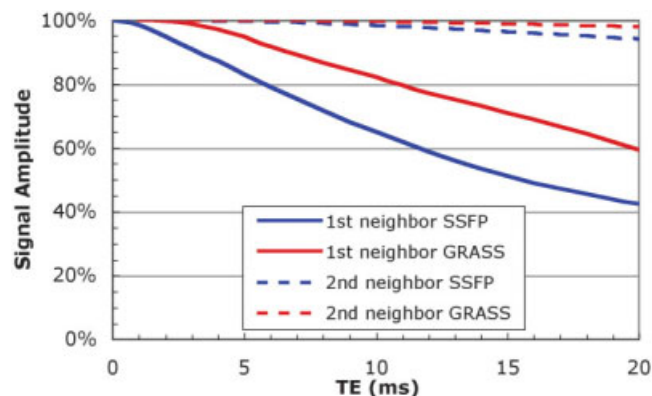


Figure 6. Simulated signal amplitude of SSFP and GRASS in the two voxels nearest the one occupied by the trabecula.

Table 3
MR-Derived Structural Parameters from Two Intact Specimens*

| | FLASE | SSFP | GRASS ^a |
|--------------------------------|------------------|--------------------------|--------------------------|
| TB thickness (μm) | | | |
| Radius 1 | 89.5 \pm 19.2 | 137.6 \pm 50.7 (+53.8) | NA |
| Radius 2 | 110.0 \pm 29.6 | 146.6 \pm 53.4 (+33.2) | 132.5 \pm 49.7 (+10.6) |
| BVF ^b | | | |
| Radius 1 | 0.090 | 0.191 (+112.2) | NA |
| Radius 2 | 0.158 | 0.214 (+35.4) | 0.196 (+19.4) |

*Numbers in parentheses represent percent differences relative to the values obtained with FLASE.

^aFrom Specimen 2, based on an additional longer scan to achieve sufficient SNR for analysis (TE/TR = 8.2/40 msec, $N_{\text{avg}} = 10$).

^bThe SD for the BVF measurements ($N = 7$) was 1.6%.

efficiency to its gradient-echo counterparts. However, in order to be effective, the TR in FLASE must be relatively long (Fig. 4), which limits the number of slice locations that can be scanned in a clinically tolerable scan time. We attribute the superior SNR efficiency of FLASE to two salient features of this pulse sequence: The first is the acquisition of a spin echo, which results in complete rephasing at the k-space center of all spectral components, in contrast to gradient echoes (11). The second is the fractional echo acquisition, which enables the use of a low receiver bandwidth while maintaining short TEs and therefore a short duration between the excitation and the phase-reversal RF pulse. The latter is important because in order to restore the inverted magnetization (resulting from $\alpha > \pi/2$) toward equilibrium, the time between the two RF pulses has to be short relative to T_1 . Conversely, the SNR of the fractional echo may be reduced relative to a full echo because the SNR of partial k-space data is proportional to the square-root-of the k-space coverage. Hence, for FLASE, in which 61% of k-space is scanned, the SNR would be reduced to 78% as opposed to sampling of a full echo. However, when the complex conjugate symmetry is exploited to retrieve the missing data, the noise characteristics of the magnitude images behave slightly differently, resulting in as much as 84% of the full data sampling (34). Further, the gain achieved from reducing

the TE by acquiring a fractional echo more than outweighs the loss from incomplete k-space coverage.

Although the low receiver bandwidth is favorable from an SNR standpoint, it is of course more sensitive to chemical shift artifacts and possibly PSF blurring (17). A bandwidth of 32 Hz/pixel (as used in FLASE) would result in a 7-pixel shift of the water relative to the dominant lipid signal. However, in the adult skeleton, bone marrow in the distal extremities (i.e., where high-resolution imaging of TB architecture is conducted) is known to be exclusively fatty (35,36). While this could still give rise to artifacts from the small water peak that is always present, as well as from other spectral components in the fatty acid triglyceride spectrum, these peaks have at least an order of magnitude lower intensity than the dominant methylene proton signal. In fact, as pointed out in the Results section, only a minor resolved peak at approximately 4 ppm to high frequency from the methylene resonance was seen. The broadening of the PSF obtained from pixels is caused by the presence of trabeculae leading to shortened T_2^* (27,37). The resulting PSF broadening (and thus slight blurring of the images) is not present when the marrow is removed and the bone is suspended in water, since the susceptibility difference between water and bone is only about 65% of that between fat and bone (7,38). In this case the PSF does not exceed the pixel bandwidth.

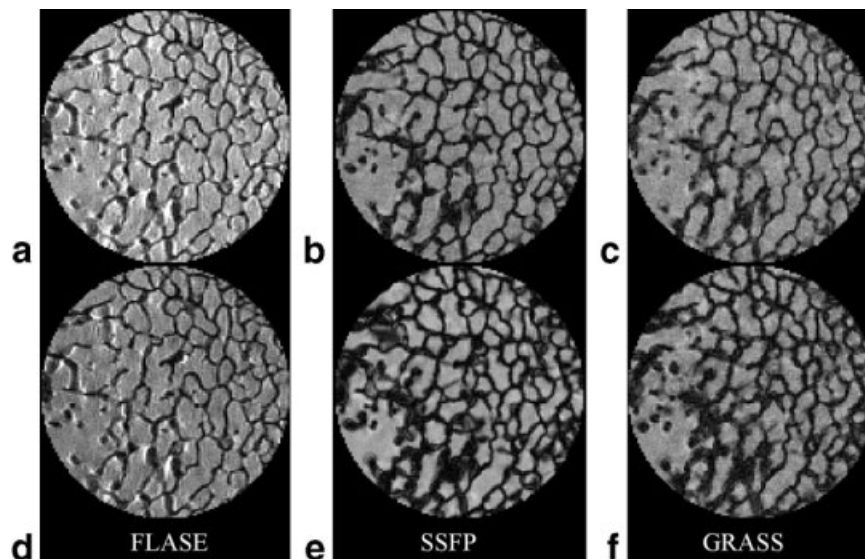


Figure 7. Images from a demarrowed specimen of TB from the distal radius, suspended in water doped with 0.9 mM Gd-DTPA at two different TEs: (a) FLASE at TE = 9.5 msec, (b) SSFP at TE = 8 msec, (c) GRASS at TE = 8 msec, and (d-f) FLASE, SSFP, and GRASS, respectively, at TE = 20 msec.

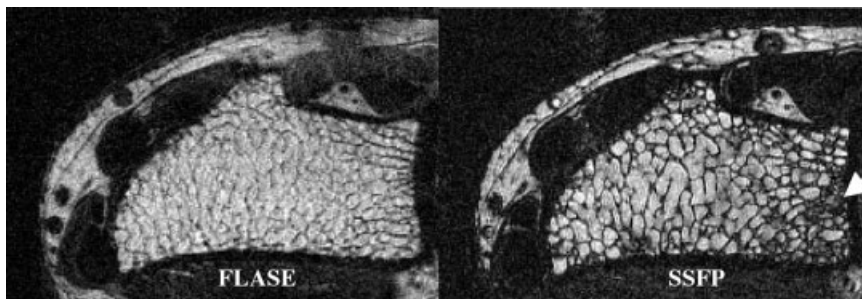


Figure 8. In vivo images of the wrist acquired with FLASE and SSFP at $156 \times 156 \times 500 \mu\text{m}^3$ voxel size. Scan time, TE, and SNR: FLASE = 12 minutes 20 seconds, TE = 9.5 msec, SNR ~ 10 ; SSFP = 3 minutes 50 seconds, TE = 8 msec, SNR ~ 5 . Note the severe overall signal loss due to off-resonance dephasing in the SSFP image near the radioulnar joint (arrow).

In doped water the SNR efficiency of SSFP is comparable to that of FLASE, in part because the T_2^* value of water is approximately the same as the T_2 . However, the SNR of all gradient-echo-based sequences (including SSFP) in edible oil drops significantly due to increased dephasing caused by the multiple spectral peaks of fat. In TB imaging, where the detected signal is from fatty bone marrow, SSFP and GRASS have about 60% and 30% lower SNRs, respectively, compared to FLASE, even though their respective TEs are actually shorter than that of FLASE. It is noteworthy that although SSFP sequences generally produce higher SNRs than GRASS for the target application, the TB may appear to be thicker because the relative signal reduction of a voxel adjacent to bone is larger in the SSFP images. This effect is supported by both the simulation results and the experimental measurements of trabecular thickness.

SSFP sequences require refocusing of all gradients and short TRs to minimize image artifacts, and hence their performance in the high-resolution regime is predominantly determined by hardware limitations. Even with the current state-of-the-art hardware of the Siemens Sonata scanner, the relatively high gradient duty cycle at the minimally allowable TR of 18 msec causes significant gradient heating and prevents the sequence from running for more than ~ 5 minutes at the resolution of $137 \times 137 \times 410 \mu\text{m}^3$. For this comparison, therefore, five separate scans had to be acquired and subsequently averaged in k-space. This mode of operation would be impractical in vivo because the pauses between averaging scans would introduce misregistration and be poorly tolerated by patients.

SSFP is well known to be highly sensitive to off-resonance effects. Aside from an inhomogeneous B_0 field, off-resonance due to chemical shift or susceptibility difference-induced local fields can lead to image artifacts manifested as reduced signal intensity or dark-bright bands. The latter could be reduced by adding two data sets acquired with constant and alternating RF phases (16) (see also Ref. 39), albeit at the expense of doubling scan time. Frequency drifts of the scanner can also cause problems, especially if there is a considerable time delay between the frequency adjustment and acquisition of the data (particularly the central k-space region), or when multiple averages are acquired when each complete data set is collected individually (as opposed to acquiring each line in k-space N_{avg} times consecutively). In the present study a frequency offset of as small as 30 Hz would introduce a 180° phase to the

evolution of the transverse signal during TR and result in severe banding artifacts in the images. In our multiple average scans, we had to readjust the scanner frequency prior to each acquisition to account for any frequency drifts that occurred. The shading of the SSFP image in Fig. 8 illustrates the difficulty of completely avoiding this effect.

In conclusion, the apparent TB thickness measured with gradient-echo-based pulse sequences was as much as 50% greater than the values obtained with FLASE. Complete rephasing of spins with FLASE in the boundary zone of the two phases of different magnetic susceptibility (i.e., bone and marrow) will yield more accurate thickness measurements, particularly when appropriate processing techniques, such as the FDT method (30), are used. Using a 2D spin-echo technique at a 9.4T field strength, Chung et al (40) showed that the bone area fraction matches the bone volume fraction measured by water displacement with a slope of 0.96 and $r^2 = 0.92$ ($P < 0.0001$). Nevertheless, despite the overall lower SNR, SSFP produces images with higher bone–bone marrow contrast, which we attribute to intravoxel spin dephasing, and therefore emphasizes trabeculae that, due to partial volume averaging, are not visible in the spin-echo images (see Fig. 8).

ACKNOWLEDGMENTS

The authors are indebted to Dr. Scott Hwang for his help in modifying the deconvolution algorithm, and Dr. Glenn Ladinsky for his assistance with the measurements of the SNR retest experiments.

REFERENCES

1. Kleerekoper M, Villanueva AR, Stanciu J, Rao DS, Parfitt AM. The role of three-dimensional trabecular microstructure in the pathogenesis of vertebral compression fractures. *Calcif Tissue Int* 1985; 37:594–597.
2. Legrand E, Chappard D, Pascaretti C, et al. Trabecular bone microarchitecture, bone mineral density, and vertebral fractures in male osteoporosis. *J Bone Miner Res* 2000;15:13–19.
3. Majumdar S. Magnetic resonance imaging of trabecular bone structure. *Top Magn Reson Imaging* 2002;13:323–334.
4. Wehrli FW, Saha PK, Gomberg BR, et al. Role of magnetic resonance for assessing structure and function of trabecular bone. *Top Magn Reson Imaging* 2002;13:335–355.
5. Parfitt AM, Mathews CH, Villanueva AR, Kleerekoper M, Frame B, Rao DS. Relationships between surface, volume, and thickness of iliac trabecular bone in aging and in osteoporosis. Implications for the microanatomic and cellular mechanisms of bone loss. *J Clin Invest* 1983;72:1396–1409.

6. Fernandez-Seara MA, Wehrli SL, Wehrli FW. Diffusion of exchangeable water in cortical bone studied by nuclear magnetic resonance. *Biophys J* 2002;82:522-529.
7. Hopkins JA, Wehrli FW. Magnetic susceptibility measurement of insoluble solids by NMR: magnetic susceptibility of bone. *Magn Reson Med* 1997;37:494-500.
8. Yablonskiy DA, Haacke EM. Theory of NMR signal behavior in magnetically inhomogeneous tissues: the static dephasing regime. *Magn Reson Med* 1994;32:749-763.
9. Reichenbach JR, Venkatesan R, Yablonskiy DA, Thompson MR, Lai S, Haacke EM. Theory and application of static field inhomogeneity effects in gradient-echo imaging. *J Magn Reson Imaging* 1997;7:266-279.
10. Ford JC, Wehrli FW, Chung HW. Magnetic field distribution in models of trabecular bone. *Magn Reson Med* 1993;30:373-379.
11. Jara H, Wehrli FW, Chung H, Ford JC. High-resolution variable flip angle 3D MR imaging of trabecular microstructure in vivo. *Magn Reson Med* 1993;29:528-539.
12. Duerk JL, Lewin JS, Wendt M, Petersilge C. Remember true FISP? A high SNR, near 1-second imaging method for T2-like contrast in interventional MRI at .2 T. *J Magn Reson Imaging* 1998;8:203-208.
13. Jung BA, Hennig J, Scheffler K. Single-breathhold 3D-trueFISP cine cardiac imaging. *Magn Reson Med* 2002;48:921-925.
14. Barkhausen J, Quick HH, Lauenstein T, et al. Whole-body MR imaging in 30 seconds with real-time true FISP and a continuously rolling table platform: feasibility study. *Radiology* 2001;220:252-256.
15. Fuchs F, Laub G, Othomo K. TrueFISP—technical considerations and cardiovascular applications. *Eur J Radiol* 2003;46:28-32.
16. Haacke EM, Brown RW, Thompson MR, Venkatesan R. *Magnetic resonance imaging: physical principles and sequence design*. New York: John Wiley & Sons, Inc., 1999. 914 p.
17. Ma J, Wehrli FW, Song HK. Fast 3D large-angle spin-echo imaging (3D FLASE). *Magn Reson Med* 1996;35:903-910.
18. Techawiboonwong A, Song HK, Saha PK, Wehrli FW. Relative performance of FLASE, TrueFISP and gradient echo in μ -MRI of trabecular bone. In: *Proceedings of the 12th Annual Meeting of ISMRM, Kyoto, Japan, 2004*. Abstract 802.
19. Pauly J, Le Roux P, Nishimura D, Macovski A. Parameter relations for the Shinnar-Le Roux selective excitation pulse design algorithm [NMR imaging]. *IEEE Trans Med Imaging* 1991;10:53-65.
20. Song HK, Wehrli FW. In vivo micro-imaging using alternating navigator echoes with applications to cancellous bone structural analysis. *Magn Reson Med* 1999;41:947-953.
21. Sekihara K. Steady-state magnetizations in rapid NMR imaging using small flip angles and short repetition intervals. *IEEE Trans Med Imaging* 1987;MI-6:157-164.
22. Oppelt A, Grauman R, Barfuss H, Fischer H, Hartl W, Schajor W. FISP—a new fast MRI sequence. *Electromedica* 1986;54:15-19.
23. Zur Y, Wood ML, Neuringer LJ. Spoiling of transverse magnetization in steady-state sequences. *Magn Reson Med* 1991;21:251-263.
24. Epstein FH, Mugler 3rd JP, Brookeman JR. Spoiling of transverse magnetization in gradient-echo (GRE) imaging during the approach to steady state. *Magn Reson Med* 1996;35:237-245.
25. MacFall JR, Pelc NJ, Vavrek RM. Correction of spatially dependent phase shifts for partial Fourier imaging. *Magn Reson Imaging* 1988;6:143-155.
26. Majumdar S. Quantitative study of the susceptibility difference between trabecular bone and bone marrow: computer simulations. *Magn Reson Med* 1991;22:101-110.
27. Majumdar S, Thomasson D, Shimakawa A, Genant HK. Quantitation of the susceptibility difference between trabecular bone and bone marrow: experimental studies. *Magn Reson Med* 1991;22:111-127.
28. Majumdar S, Newitt D, Jergas M, et al. Evaluation of technical factors affecting the quantification of trabecular bone structure using magnetic resonance imaging. *Bone* 1995;17:417-430.
29. Wehrli FW, Hwang SN, Ma J, Song HK, Ford JC, Haddad JG. Cancellous bone volume and structure in the forearm: noninvasive assessment with MR microimaging and image processing. *Radiology* 1998;206:347-357.
30. Saha PK, Wehrli FW. Measurement of trabecular bone thickness in the limited resolution regime of in vivo MRI by fuzzy distance transform. *IEEE Trans Med Imaging* 2004;23:53-62.
31. Chung HW, Hwang SN, Yeung HN, Wehrli FW. Mapping of the magnetic-field distribution in cancellous bone. *J Magn Reson Ser B* 1996;113:172-176.
32. Bakker CJ, Bhagwandien R, Moerland MA, Ramos LM. Simulation of susceptibility artifacts in 2D and 3D Fourier transform spin-echo and gradient-echo magnetic resonance imaging. *Magn Reson Imaging* 1994;12:767-774.
33. Schenck JF. The role of magnetic susceptibility in magnetic resonance imaging: MRI magnetic compatibility of the first and second kinds. *Med Phys* 1996;23:815-850.
34. Hua J, Hurst GC, Duerk JL. Some noise properties of 2DFT MR images from asymmetrically sampled data. *Med Phys* 1992;19:1191-1194.
35. Dooms GC, Fisher MR, Hricak H, Richardson M, Crooks LE, Genant HK. Bone marrow imaging: magnetic resonance studies related to age and sex. *Radiology* 1985;155:429-432.
36. Koo KH, Dussault R, Kaplan P, et al. Age-related marrow conversion in the proximal metaphysis of the femur: evaluation with T1-weighted MR imaging. *Radiology* 1998;206:745-748.
37. Wehrli FW, Ford JC, Attie M, Kressel HY, Kaplan FS. Trabecular structure: preliminary application of MR interferometry. *Radiology* 1991;179:615-621.
38. Wehrli FW, Ford JC, Haddad JG. Osteoporosis: clinical assessment with quantitative MR imaging in diagnosis. *Radiology* 1995;196:631-641.
39. Banerjee S, Han ET, Krug R, Newitt DC, Majumdar S. Application of refocused steady-state free-precession methods at 1.5 and 3 T to in vivo high-resolution MRI of trabecular bone: simulations and experiments. *J Magn Reson Imaging* 2005;21:818-825.
40. Chung HW, Wehrli FW, Williams JL, Kugelmass SD, Wehrli SL. Quantitative analysis of trabecular microstructure by 400 MHz nuclear magnetic resonance imaging. *J Bone Miner Res* 1995;10:803-811.